OPEN ACCESS

Energy Storage ARTICLE

The Innovation Energy

Deformation-adaptive polyurethane-based LLZO composite solid electrolytes: Design and performance

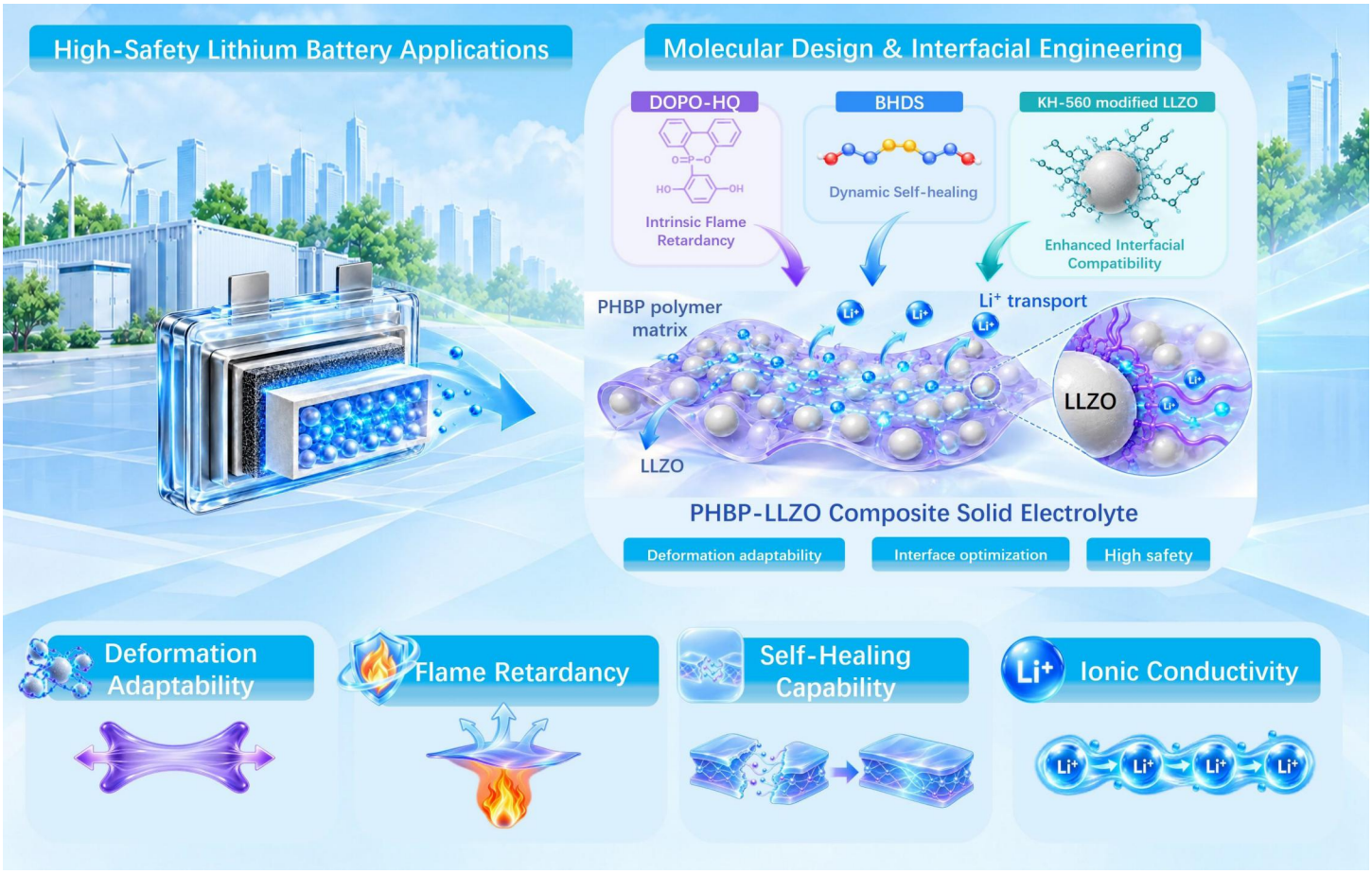
Ke-Xin Huang,[1,2] Da-Yong Wu,[1,*] Jian-Hua Cao,[1] Yue Li,[1] and Jun Shen[1]

*Correspondence: dayongwu@mail.ipc.ac.cn

Received: June 26, 2026; Accepted: September 28, 2026; Published Online: October 20, 2026; https://doi.org/10.59717/j.xinn-energy.2026.100193

© 2026 The Author(s). This is an open access article under the CC BY license (https://creativecommons.org/licenses/by/4.0/).

GRAPHICAL ABSTRACT



PUBLIC SUMMARY

- A synergistic molecular-interface engineering strategy was proposed.
- Intrinsic flame retardancy and self-healing were integrated into one electrolyte.
- Covalent PU-(KH-560)-LLZO interfaces enabled fast and stable Li^+ transport.

ARTICLE Energy Storage

OPEN ACCESS

www.the-innovation.org/the-innovation-energy

Deformation-adaptive polyurethane-based LLZO composite solid electrolytes: Design and performance

Ke-Xin Huang,[1,2] Da-Yong Wu,[1,*] Jian-Hua Cao,[1] Yue Li,[1] and Jun Shen[1]

[1]Technical Institute of Physics and Chemistry, Chinese Academy of Sciences, Beijing 100190, China

[2]University of Chinese Academy of Sciences, Beijing 100049, China

*Correspondence: dayongwu@mail.ipc.ac.cn

Received: June 26, 2026; Accepted: September 28, 2026; Published Online: October 20, 2026; https://doi.org/10.59717/j.xinn-energy.2026.100193

© 2026 The Author(s). This is an open access article under the CC BY license (https://creativecommons.org/licenses/by/4.0/).

Citation: Huang K., Wu D., Cao J., et al. (2026). Deformation-adaptive polyurethane-based LLZO composite solid electrolytes: Design and performance. *The Innovation Energy* **3**:100193.

Polyurethane (PU)-based solid-state electrolytes confront several inherent limitations, including inferior interfacial compatibility with inorganic fillers, insufficient mechanical robustness, poor flame retardancy, and weak suppression of lithium dendrite growth. Herein, we construct a phosphorus-containing flame-retardant and dynamically self-healing dual-functional polyurethane-based $Li_7La_3Zr_2O_{12}$ (LLZO) composite solid electrolyte (PHBP-LLZO) via a synergistic strategy of molecular structure design and interfacial engineering. The introduction of a phosphorus-containing flame-retardant monomer (DOPO-HQ) and a dynamic disulfide-bridged chain extender (BHDS) endows the PU matrix with intrinsic flame retardancy and reversible self-healing capability. Meanwhile, surface modification of LLZO using the silane coupling agent KH-560 establishes robust covalent Si–O–Zr linkages at the organic-inorganic interface, improving the dispersibility and interfacial compatibility of LLZO fillers. The optimized PHBP-LLZO composite membrane achieves superior comprehensive performance, including excellent mechanical toughness (a tensile strength of 19.8 MPa and an elongation at break of 988%), intrinsic flame retardancy, and reliable self-healing capability. It also delivers a high ionic conductivity of 2.03×10^{-4} S·cm^{-1}, a broad electrochemical stability window of 5.05 V (vs. Li^+/Li), and prominent lithium dendrite inhibition ability. The assembled LFP||Li quasi-solid-state battery retains a capacity retention rate of 70.3% after 300 continuous cycles at 0.5 C. Moreover, the Li||Li symmetric cell realizes stable long-term cycling for over 1200 h at a current density of 0.1 mA·cm^{-2}. This work offers a novel molecular-interfacial synergistic design strategy for composite electrolytes in high-safety quasi-solid-state lithium batteries.

INTRODUCTION

All-solid-state lithium batteries (ASSLBs) are widely regarded as a promising technology for overcoming the energy density and safety limitations of conventional liquid-based lithium batteries. Among their key enabling components, high-performance solid-state electrolytes and scalable processing technologies are essential for practical application.[1-4] Inorganic ceramic electrolytes possess high ionic conductivity and mechanical strength, but they generally suffer from severe brittleness, poor machinability, and inferior interfacial contact with electrodes.[5-8] In contrast, organic polymer electrolytes exhibit excellent flexibility and processability, but their applications are constrained by low room-temperature ionic conductivity and insufficient thermal stability.[9,10] Consequently, organic–inorganic composite solid electrolytes (CSEs), which integrate the respective advantages of both ceramic and polymer components, have emerged as one of the most promising approaches for balancing electrochemical performance and processability.[11-15]

Despite the considerable promise of CSEs, their performance remains constrained by interrelated scientific and engineering challenges. From an intrinsic material perspective, the major barriers to efficient Li^+ transport include poor interfacial compatibility between the organic and inorganic phases, high interfacial resistance, and discontinuous Li^+ transport pathways across the two phases.[16,17] From a manufacturing perspective, inorganic fillers tend to agglomerate, while pores and interfacial defects are readily generated during membrane fabrication, further compromising structural integrity and degrading both electrochemical and mechanical performance. In CSE systems, the polymer matrix not only serves as a vital medium for Li^+ transport but also fulfills multiple additional roles, including dispersing inorganic fillers, accommodating electrode interfaces, and maintaining the structural integrity of the membrane. Its molecular structure, segmental mobility, and interfacial interactions collectively determine the overall performance of CSEs.[18] Consequently, developing well-matched polymer matrices and engineering robust organic-inorganic interfacial interactions are essential strategies for enhancing the overall performance of CSEs.

Currently, commonly used polymer systems include polyethers (e.g., poly(ethylene oxide), PEO),[19-21] fluoropolymers (e.g., poly(vinylidene fluoride)/poly(vinylidene fluoride-co-hexafluoropropylene), PVDF/PVDF-HFP),[22-24] polynitriles (e.g., PAN),[25-27] and methacrylates (e.g., PMMA).[28-30] Among them, PEO has become the most widely studied matrix material due to its excellent lithium salt dissolution capability and good interfacial adhesion. However, its high crystallinity restricts segmental mobility, resulting in room-temperature ionic conductivity insufficient for practical application.[31,32] PVDF-based polymers exhibit a high dielectric constant and excellent thermal stability, yet they suffer from limited interfacial compatibility with lithium metal anodes and are prone to dehydrofluorination side reactions during cycling. Although PAN and PMMA can enhance ionic conductivity to a certain extent, they are limited by inherent brittleness and relatively narrow electrochemical stability windows. Overall, no single polymer system is capable of simultaneously delivering high-performance ionic transport, superior mechanical properties, thermal safety and interfacial stability. Therefore, multi-performance synergy must be achieved through molecular structure design and composite modification.

Polyurethane (PU), featuring a unique microphase-separated structure consisting of soft and hard segments, combines excellent flexibility with high mechanical robustness, making it a promising polymer matrix for solid-state electrolytes.[33,34] However, conventional PU-based solid-state electrolytes continue to face four major bottlenecks: low room-temperature ionic conductivity (typically ~10^{-6} S·cm^{-1}),[35] insufficient intrinsic flame retardancy, poor interfacial compatibility with inorganic ceramic fillers, and the inherent trade-off between mechanical strength and ionic transport. These limitations significantly hinder their application in high-safety solid-state lithium batteries.[36,37]

To address the above challenges, substantial efforts have been devoted to improving the performance of PU-based solid-state electrolytes through diverse modification strategies. For enhancing ionic conductivity, Wang et al.[38] suppressed PU crystallization via constructing a hyperbranched PU structure combined with ionic liquid plasticization, elevating the room-temperature ionic conductivity to 4×10^{-4} S·cm^{-1}. The assembled lithium iron phosphate (LFP)-based cell delivered a capacity retention of 83% after 1000 cycles at 0.5 C. Gao et al.[39] incorporated 4 wt% LLZTO into the PU matrix, resulting in a room-temperature ionic conductivity of 2.22×10^{-4} S·cm^{-1}, a lithium-ion transference number of 0.55, and an electrochemical stability window of 5.0 V. Huang et al.[40] enhanced interfacial interactions through the incorporation of amino-functionalized UiO-66-NH_2 fillers. The resulting PU composite electrolyte exhibited a room-temperature ionic conductivity of 2.1×10^{-4} S·cm^{-1} and a high lithium-ion transference number of 0.71, leading to significantly improved cycling stability. To improve thermal safety, Wu et al.[37] covalently grafted bromine-containing flame-retardant monomers onto the PU backbone. The resulting electrolyte self-extinguished after 6 s of flame exposure, and the corresponding batteries matched with high-nickel cathodes exhibited outstanding cycling performance. From the perspective of functional structural design, Elizalde et al.[41] synthesized poly(urea-urethane)

Table 1. Feed composition for the synthesis reactions

Materials Product	PEG2000	BHDS	DOPO-HQ	HDI	DMF	R	Film formation
PHB 1	4 g 2.0 mmol	200 μL 1.48 mmol	—	0.535 mL 3.31 mmol	20 mL	R=0.95	good
PHB 2	4 g 2.0 mmol	200 μL 1.48 mmol	—	0.563 mL 3.48 mmol	20 mL	R=1	NG
PHB 3	4 g 2.0 mmol	200 μL 1.48 mmol	—	0.591 mL 3.65 mmol	20 mL	R=1.05	NG
PHB 4	4 g 2.0 mmol	100 μL 0.74 mmol	—	0.421 mL 2.60 mmol	20 mL	R=0.95	NG
PHB 5	4 g 2.0 mmol	300 μL 2.22 mmol	—	0.648 mL 4.01 mmol	20 mL	R=0.95	good
PHB 6	4 g 2.0 mmol	400 μL 2.96 mmol	—	0.762 mL 4.71 mmol	20 mL	R=0.95	NG
PHBP 1	4 g 2.0 mmol	200 μL 1.48 mmol	0.3 g 0.93 mmol	0.677 mL 4.19 mmol	20 mL	R=0.95	good
PHBP 2	4 g 2.0 mmol	200 μL 1.48 mmol	0.5 g 1.54 mmol	0.771 mL 4.77 mmol	20 mL	R=0.95	good
PHBP 3	4 g 2.0 mmol	200 μL 1.48 mmol	0.7 g 2.16 mmol	0.866 mL 5.36 mmol	20 mL	R=0.95	NG

electrolytes containing dynamic hindered urea bonds to endow the material with self-healing capability, effectively stabilizing interfacial contact during cycling.

However, existing modification strategies for PU-based electrolytes are mostly focused on optimizing a single property, making it difficult to simultaneously achieve the synergistic combination of high-efficiency ionic transport, intrinsic flame retardancy, dynamic self-healing, and interfacial stability. Moreover, the microscopic interaction mechanism at the organic-inorganic interface remains insufficiently understood and requires further clarification. Beyond the molecular design of the bulk material, the fabrication technology is another critical determinant of the microstructure and macroscopic performance of CSEs. Current preparation methods for CSEs are broadly classified into wet and dry processing routes.[42] Wet processing, represented by solution casting and doctor-blade coating, is simple to operate. However, during solvent evaporation, the polarity difference between the organic and inorganic phases tends to induce phase separation, leading to filler aggregation and interfacial defects.[43] To address this issue, Zhang et al.[44] constructed covalent bridges between the PVDF-HFP matrix and LLZTO fillers using the silane coupling agent IPTS, which significantly improved filler dispersion and increased the room-temperature ionic conductivity of the composite electrolyte to 0.6 $mS{\cdot}cm^{-1}$, with a lithium-ion transference number of 0.87. Although dry processing enables solvent-free fabrication,[45] it still suffers from several key limitations, including poor film flexibility, limited scalability, high manufacturing cost, and difficulty in achieving uniform thickness control, which currently hinder its large-scale application. In summary, on the basis of mature wet-processing technologies, the synergistic integration of molecular design and interfacial engineering to address filler dispersion and interfacial resistance issues represents a practical and effective strategy for developing high-performance CSEs.

In light of the above research background and existing bottlenecks, we herein propose a synergistic modification strategy integrating molecular functional design with interfacial covalent bridging to construct a polyurethane-based LLZO composite solid electrolyte (PHBP-LLZO) that combines flame retardancy, self-healing capability, and high-efficiency Li^+ transport. Specifically, the phosphorus-containing flame-retardant monomer DOPO-HQ and the dynamic disulfide-containing chain extender BHDS are incorporated into the PU backbone via copolymerization, thereby simultaneously imparting intrinsic flame retardancy and thermally induced self-healing capability to the polymer matrix. Meanwhile, the LLZO inorganic filler is surface-modified with the silane coupling agent KH-560 to construct Si–O–Zr covalent bridges at the organic-inorganic interface, effectively reinforcing interfacial interactions and promoting uniform filler dispersion. This interfacial engineering further reduces interfacial resistance and enables continuous Li^+ transport pathways across the composite electrolyte.

MATERIALS AND METHODS

Materials

Polyethylene glycol (PEG, Mw = 2000 $g{\cdot}mol^{-1}$), hexamethylene diisocyanate (HDI, 99%, AR), dibutyltin dilaurate (DBTDL, 95%), N,N-dimethylformamide (DMF, 99%, AR), 10-(2,5-dihydroxyphenyl)-10H-9-oxa-10-phosphaphenanthrene-10-oxide (DOPO-HQ, 95%), bis(2-hydroxyethyl) disulfide (BHDS, 98%), and anhydrous ethanol were all purchased from Aladdin Biochemical Technology Co., Ltd. (3-Glycidyloxypropyl)trimethoxysilane (KH-560) was purchased from Sigma-Aldrich. Lithium bis(trifluoromethanesulfonyl)imide (LiTFSI), dimethyl carbonate (DMC, AR), and electrolyte LB-149 were purchased from Suzhou Duoduo Chemical Technology Co., Ltd. Lithium foil (0.45 mm) was purchased from Kelude New Energy Technology Co., Ltd. $Li_7La_3Zr_2O_{12}$ (LLZO), $LiFePO_4$ (LFP), acetylene black, and poly(vinylidene fluoride) (PVDF, HSV900) were purchased from Shenzhen Kejing Star Technology Co., Ltd. The LLZO and LFP powder were vacuum-dried at 80 °C for 12 h prior to use. All other reagents were used as received without further purification.

Synthesis and Preparation

The target polymer was synthesized in three batches, each employing a different feed ratio to enable comparison of the film formation ability differences among the resulting products (Table 1). Figure 1 illustrates the synthetic route along with the optimized feed ratio.

Synthesis and Condition Optimization of Polyurethanes. PEG-HDI-BHDS(PHB): PEG2000 was placed in a 100 mL three-neck flask under a nitrogen atmosphere and heated to 110 °C in an oil bath for 1 h. After cooling to 80 °C, DMF, HDI, and the catalyst DBTDL were sequentially introduced, and the mixture was stirred mechanically for 2 h. Subsequently, the chain extender BHDS was added, and the reaction was continued for an additional 6 h. During the later stages of the reaction, additional DMF was periodically added at 2 h intervals. After completion, a colorless transparent PHB solution was obtained. After optimization, PHB-1 which exhibited a viscosity of 6.67 Pa·s and a weight-average molecular weight (Mw) of 1.1×10^5 $g{\cdot}mol^{-1}$ was selected for subsequent experiments.

PHB-HDI-BHDS-(DOPO-HQ) (PHBP): PEG2000 and DOPO-HQ were first added to a 100 mL three-neck flask under a nitrogen atmosphere and heated to 110 °C in an oil bath for 1 h. After cooling to 80 °C, DMF, HDI, and the catalyst DBTDL were sequentially introduced, and the mixture was stirred mechanically for 2 h. Subsequently, the chain extender BHDS was added and the reaction was continued for an additional 6 h. During the later stages of the reaction, DMF was periodically added at 2 h intervals. After completion, a colorless transparent PHBP solution was obtained. After optimization, PHBP-2, which exhibited a viscosity of 5.56 Pa·s and a weight-average molecular weight (Mw) of 5.8×10^4 $g{\cdot}mol^{-1}$, was selected for subsequent experiments.

Surface coupling modification of LLZO particles. 0.04 g of KH-560 was

dissolved in 10 mL of an anhydrous ethanol/deionized water mixture (volume ratio 9:1) and stirred at room temperature to complete hydrolysis. Subsequently, 0.4 g of LLZO powder was added and the suspension was stirred at 60 °C for 2 h. After reaction, the product was collected by filtration, washed three times with ethanol, and vacuum-dried at 60 °C for 12 h. The resulting silane-functionalized LLZO particles, denoted as KH-560/LLZO, were stored in a desiccator prior to use.

Organic-Inorganic Composite Solid Electrolyte. Preparation of PHBP-LLZO composite solid-state electrolyte membrane: In an argon-filled glovebox (both H_2O and O_2 levels below 0.1 ppm), 10 mL of DMF was mixed with 0.72 g of PHBP solid and stirred until complete dissolution. Subsequently, 0.48 g of modified LLZO (PHBP:LLZO mass ratio = 1.5:1) and 0.188 g of LiTFSI ([EO]:[Li^+] molar ratio = 18:1) were added. The mixture was then stirred (50 °C, 5 h) and vacuum-defoamed to yield a homogeneously dispersed slurry. The slurry was cast into a 6 cm × 6 cm PTFE mold, evenly spread, and transferred to a vacuum oven at 60 °C for drying for 24 h. A PHBP-LLZO composite solid-state electrolyte membrane with a thickness of 150 μm was finally obtained and labeled as PHBP-LLZO.

Preparation of control samples: For comparison, PHB and PHBP polymer solutions were separately mixed with LiTFSI, with the polymer solid content controlled at 2 g in each case and the [EO]:[Li^+] molar ratio maintained at 18:1. The corresponding pure PHB and PHBP solid-state electrolyte membranes were prepared following the same procedure described above.

Self-Healing Performance Test

The electrolyte membrane was fully cut into two pieces using a surgical blade. The two fractured surfaces were brought into intimate contact and aligned and then annealed in a thermostatic oven at 60 °C for 1 h. The tensile strength of the membrane before and after healing was measured using a universal testing machine to evaluate its self-healing efficiency.

Flame Retardancy Test

The flame retardancy of the solid-state electrolyte membrane was evaluated using a direct flame exposure method. The membrane was exposed to the flame of an alcohol lamp, and the ignition time, burning rate, self-extinguishing time, and morphology of the combustion residue were recorded to comprehensively assess its flame-retardant performance.

Battery Assembly

In an argon-filled glovebox (O_2 < 0.1 ppm, H_2O < 0.1 ppm), CR2032-type coin cells were assembled using an LFP cathode, the solid-state electrolyte membrane, and a lithium metal anode. During assembly, 2.5 μL of electrolyte was drop-cast onto each side of the electrolyte membrane (5 μL in total) to improve interfacial wetting and reduce interfacial resistance. $LiFePO_4$, acetylene black, and poly(vinylidene fluoride) (PVDF) were uniformly dispersed in N-methyl-2-pyrrolidone (NMP) at a mass ratio of 8:1:1 to prepare the cathode slurry with a solid content of 23.8%. The slurry was then uniformly coated onto an aluminum foil current collector, followed by drying at 60 °C for 7 h and hot pressing at 70 °C. The resulting electrode was punched into circular cathodes with a diameter of 13 mm. Prior to use, the cathodes were further vacuum-dried at 120 °C for 12 h and subsequently transferred to an argon-filled glovebox for storage. The prepared cathodes had two different active-material loadings of 2 and 4 mg·cm^{-2}.

Characterization and Measurements

The molecular weight and molecular weight distribution of the polyurethanes were determined by gel permeation chromatography (GPC, Waters GPC2695, USA). The surface and cross-section morphology of the samples was examined using a field-emission scanning electron microscope (FESEM, S-4800, Hitachi, Japan) at an accelerating voltage of 10 kV. The crystal structures of the electrolyte membranes were characterized by X-ray diffraction (XRD, D8 Focus, Bruker, Germany) using Cu Kα radiation over a 2θ range of 10°-70°. The thermal decomposition temperature was determined according to previously reported methods.[46] The mechanical properties of the samples were evaluated using a universal testing machine (Instron 5966, USA), with five independent measurements performed for each sample and the average value reported. Thermomechanical analysis (TMA, Q400, TA Instruments, USA) was performed to evaluate the thermally induced dimensional changes of the electrolyte membranes upon heating. The measurements were conducted over a temperature range of −90 to 150 °C in compression mode, with a preload force of 0.05 N and a heating rate of 5 °C·min^{-1}. Thermogravimetric analysis coupled with Fourier transform infrared spectroscopy (TG-IR, TGA 4000 + SP2, PerkinElmer, USA) was employed to analyze the composition and evolution of volatile gaseous products generated during the thermal decomposition of the samples. The glass-transition and melting behaviors of the electrolyte membranes were characterized using differential scanning calorimetry (DSC, DSC 25, TA Instruments, USA). The electrochemical properties of the electrolyte membranes, including ionic conductivity, electrochemical stability window, and lithium-ion transference number, were measured using an electrochemical workstation (Zennium 6, Zahner, Germany) under conditions described in previous studies.[47] The cycling and rate performance of the assembled coin cells were evaluated on a LAND battery testing system (CT2001A, LAND, Wuhan, China) over a voltage range of 2.5-3.6 V at 25 °C. After cycling, the cells were disassembled in an argon-filled glovebox, and the lithium anodes were rinsed with DMC and dried. The elemental composition of lithium anodes was analyzed by X-ray photoelectron spectroscopy (XPS, ESCALAB 250Xi, UK).

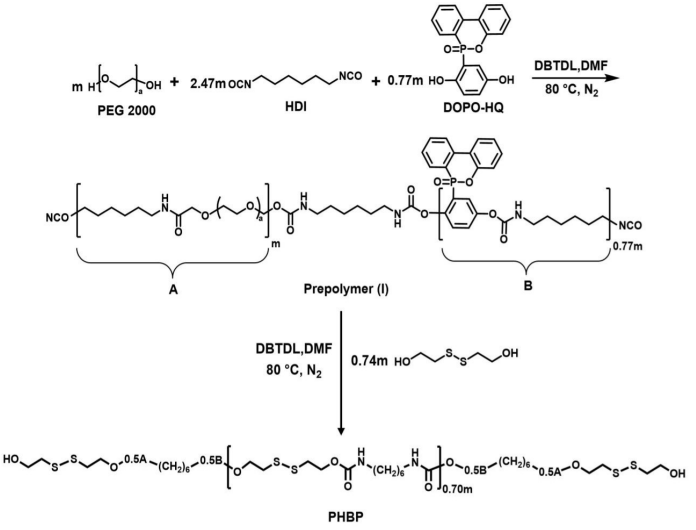


Figure 1. Synthetic route of PHBP

Theoretical Calculations

All density functional theory (DFT) calculations were performed using the Gaussian 16 software package. Geometry optimizations and vibrational frequency analyses were carried out at the B3LYP level of theory with Grimme's D3 dispersion correction (EmpiricalDispersion = GD3) to account for noncovalent interactions. All optimized structures were confirmed to be true minima on the potential energy surface, with no imaginary frequencies observed.

For the organic molecular systems, including PEG (modeled by diethylene glycol dimethyl ether as an oligomeric analogue), BHDS, and DOPO-HQ, the 6-31+G(d,p) basis set was consistently employed. Molecular electrostatic potential (ESP) analyses were performed on the optimized structures using Multiwfn 3.8,[48] based on electron density isosurfaces at 0.001 a.u. The ESP distributions were visualized on van der Waals surfaces. The corresponding molecular surface images were rendered using VMD 1.9.3,[49] with a uniform color scale applied within each system.

Li^+ Binding Energy. The binding energy between Li^+ and each molecule was calculated at the same theoretical level. The Li^+-molecule complex was first subjected to geometry optimization, and the binding energy E_b was subsequently calculated according to the following equation:

$$E_b = E_{complex} - (E_{molecule} + E_{Li^+})$$

where $E_{complex}$ is the total energy of the complex, $E_{molecule}$ is the total energy of the isolated molecule, and E_{Li^+} is the total energy of the isolated lithium ion.

Calculation of the Interfacial Interactions of KH-560/LLZO and KH-560/PU. To elucidate the mechanistic role of the silane coupling agent KH-560 at the organic-inorganic interface, DFT calculations were performed to analyze its interaction with the inorganic filler surface. A composite structure was constructed between the KH-560 molecule and a simplified zirconium-oxygen coordination polyhedral cluster, which serves as a representative model for the LLZO surface. For systems involving the transition metal Zr, the 6-31G(d) basis set was employed for light elements (C, H, O, Si), while the LANL2DZ effective core potential (ECP) basis set was adopted for the Zr atoms. After geometry optimization was performed to obtain the stable configuration, the strength of the chemical condensation interaction was evaluated by calculating the interfacial binding energy, expressed as follows:

$$E_{bind}=E_{interface}-(E_{KH\text{-}560}+E_{surface})$$

where $E_{interface}$ is the total energy of the composite structure formed by KH-560 and the inorganic surface, and $E_{KH\text{-}560}$ and $E_{surface}$ are the energies of the individual components.

Meanwhile, to assess the interaction between KH-560 and the polymer matrix, a molecular fragment containing the urethane group was selected as a representative model for polyurethane, and a composite structure between KH-560 and the polymer fragment was constructed for comparative analysis. For the calculation of the binding energy of this physisorption system, the counterpoise (CP) method was employed to eliminate the basis set superposition error (BSSE).

Bond Dissociation Enthalpy of DOPO-HQ. To investigate the flame-retardant role of DOPO-HQ in the PHBP matrix, the bond dissociation enthalpy (BDE) of key chemical bonds in the molecule was calculated. The DOPO-HQ molecule and the radical fragments generated upon bond cleavage were first subjected to geometry optimization and frequency analysis, and the BDE at 298 K was subsequently calculated according to the following equation:

$$BDE = [H(Radical_1) + H(Radical_2)] - H(DOPO\text{ - }HQ)$$

This equation gives the bond dissociation enthalpy for the homolytic cleavage of a specific chemical bond in the DOPO-HQ molecule, with the enthalpy values derived from the thermodynamic parameters obtained from the frequency calculations.

The reaction can be expressed as:

$$DOPO-HQ \rightarrow Radical_1 + Radical_2$$

RESULTS AND DISCUSSION

Synthesis Strategy of PHBP

The target polyurethane (PHBP) was synthesized via step-growth polymerization between isocyanate (–NCO) and hydroxyl groups (–OH), using polyethylene glycol (PEG2000), hexamethylene diisocyanate (HDI), bis(2-hydroxyethyl) disulfide (BHDS), and the phosphorus-containing flame-retardant monomer DOPO-HQ as raw materials. The physical properties of the polymer are governed by molecular weight, the arrangement and length of structural units, and terminal functional groups. Moreover, the ability to form a well-compatible interface between the polymer and inorganic components is a key factor determining the performance of the resulting composites. During synthesis, a prepolymer was first formed from PEG, HDI, and DOPO-HQ, followed by chain extension with BHDS, which simultaneously introduced disulfide-containing dynamic units, ultimately yielding a hydroxyl-terminated product. The feed ratios of the raw materials were optimized to achieve a balance between film-forming capability and mechanical toughness.

The film-forming properties and overall performance of the polymer were systematically optimized by adjusting the isocyanate index *(R)* and feed ratios of functional monomers. At $R = 1$ and $R = 1.05$, the degree of crosslinking was excessively high, resulting in significant embrittlement after film formation. The optimal film-forming performance was achieved at $R = 0.95$ (Figure S1), and all subsequent optimizations of functional monomer compositions were carried out under this condition. The chain extender BHDS plays a dual role in chain extension and dynamic functionalization: its terminal hydroxyl groups react with the NCO-terminated prepolymer to promote molecular chain growth and construct a crosslinked network, while the disulfide bonds in the backbone act as dynamic reversible sites, endowing the material with thermally triggered self-healing capability. At a BHDS feed amount of 100 μL **(PHB 4)**, the chain extension reaction was insufficient, resulting in an incompletely crosslinked network and insufficient disulfide bond density, preventing the formation of a freestanding membrane. At 200 μL **(PHB 1)** and 300 μL **(PHB 5)**, the degree of chain extension was moderate, yielding good film-forming ability and flexibility. When the feed amount was increased to 400 μL **(PHB 6)**, excessive crosslinking occurred, restricting segmental mobility and leading to membrane embrittlement (Table 1). Considering both film-forming performance and self-healing requirements, 200 μL was ultimately selected as the optimal BHDS feed amount. For the phosphorus-containing flame-retardant unit DOPO-HQ, an addition of 0.3 g resulted in insufficient flame-retardant element content and limited flame retardancy. At an addition of 0.7 g, the proportion of rigid aromatic structures became excessively high, which also deteriorated film-forming ability, leading to membrane brittleness.

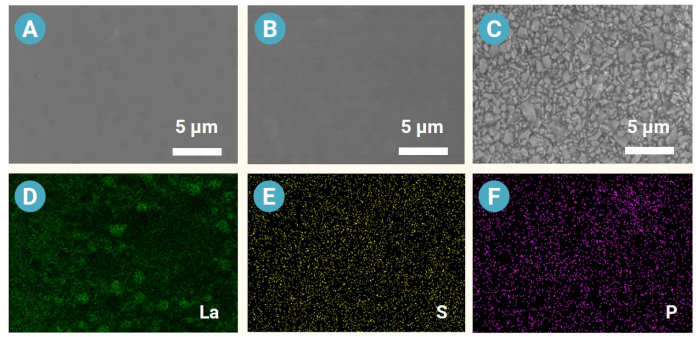


Figure 2. SEM images and EDS mapping (A) Surface morphology of the PHB membrane; (B) surface morphology of the PHBP membrane; (C) surface morphology of the PHBP-LLZO composite membrane; (D–F) EDS elemental mappings of La, S, and P in the PHBP-LLZO composite membrane.

Effect of Silane Coupling Agent on the Interfacial Regulation of PHBP-LLZO

As can be seen from Figure 2A & B, the pristine PHB and PHBP matrix membranes exhibit smooth and defect-free surfaces, indicating a well-balanced ratio between PEG-derived flexible soft segments and hard segments constructed from DOPO-HQ and BHDS, which endows the polymer with excellent film-forming capability. After incorporation of KH-560-modified LLZO inorganic particles into the PHBP matrix, the ceramic fillers are uniformly dispersed within the polymer matrix without obvious agglomeration, confirming that silane coupling modification effectively enhances the organic–inorganic interfacial compatibility (Figure 2C). The corresponding EDS elemental mapping (Figure 2D-F) reveals that La (from LLZO), S (from disulfide-based self-healing units), and P (from phosphorus-containing flame-retardant groups) are homogeneously distributed throughout the scanned area, demonstrating uniform spatial distribution of both inorganic fillers and functional moieties within the composite membrane.

FTIR results provide evidence for the successful covalent incorporation of functional monomers into the polyurethane backbone (Figure S2). The complete disappearance of the –NCO characteristic peak of HDI, together with the emergence of the N–H and C=O stretching vibrations of urethane groups, the C–O–C vibrations of PEG ether linkages, the P=O and P–O–C(aryl) signals of DOPO-HQ, and the characteristic features associated with BHDS, collectively confirm the formation of the PHBP polymer structure. The XRD patterns reveal the regulatory effect of fillers on the polymer crystallization behavior (Figure S3). Pristine PHB exhibits a single broad amorphous halo. Upon incorporation of rigid DOPO-HQ units, aromatic π–π interactions induce partial ordering of hard segments, resulting in two distinct diffraction peaks in PHBP.[50] After introduction of KH-560-modified LLZO, the steric effect of ceramic particles suppresses the ordered packing of PEG chains, leading to a pronounced decrease in crystallinity and an increased amorphous fraction, which is beneficial for Li^+ transport. Meanwhile, KH-560 modification does not alter the cubic garnet structure of LLZO, as it modifies only

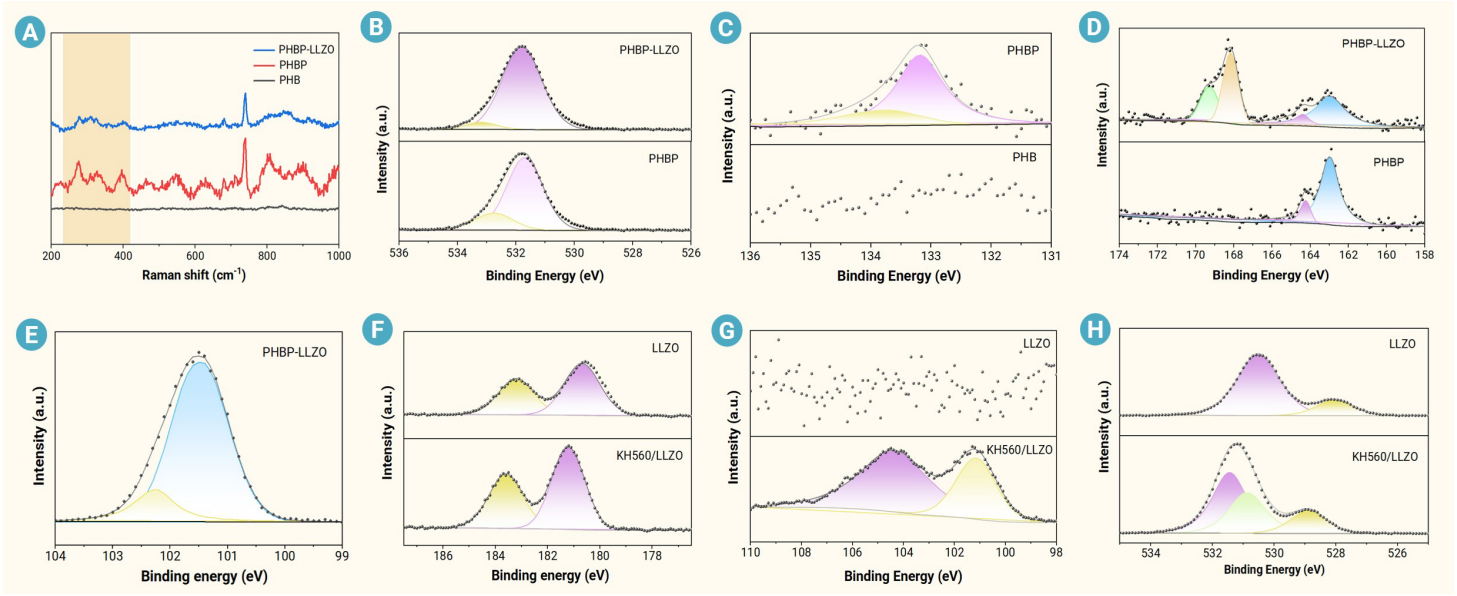


Figure 3. Characterization of compositional and interfacial chemistry of the composite membranes (A) Raman spectra of PHB, PHBP, and PHBP-LLZO; (B) high-resolution O 1s XPS spectra of PHBP and PHBP-LLZO; (C) high-resolution P 2p XPS spectra of PHB and PHBP; (D) high-resolution S 2p XPS spectra of PHBP and PHBP-LLZO; (E) high-resolution Si 2p XPS spectrum of PHBP-LLZO; (F) Zr 3d XPS spectra of LLZO and KH-560/LLZO; (G) Si 2p XPS spectra of LLZO and KH-560/LLZO; (H) O 1s XPS spectra of LLZO and KH-560/LLZO.

the particle surface without affecting the intrinsic ionic conduction framework.

Raman spectroscopy and high-resolution XPS further elucidate the interfacial interaction characteristics. As shown in Figure 3A, the characteristic Raman peaks associated with DOPO-HQ in PHBP are significantly attenuated in the PHBP-LLZO composite membrane, reflecting strong interfacial interactions between the polymer matrix and LLZO, which alter the local vibrational environment of the organic segments. XPS analysis reveals a systematic evolution of chemical states at the organic-inorganic interface. The O 1s peak of the composite membrane shifts toward higher binding energy by ~0.3 eV compared with that of PHBP, indicating a reduced electron density of oxygen atoms due to coordination between PEG ether oxygens and undercoordinated metal-oxygen sites on the LLZO surface (Figure 3B). The P 2p and S 2p spectra confirm the successful incorporation of DOPO-HQ and BHDS into the polymer backbone, respectively. Meanwhile, the emergence of high-valence sulfur species suggests that partial sulfur atoms participate in interfacial coordination interactions within the composite system (Figure 3C & D). In the Si 2p spectrum, the peaks of PHBP-LLZO can be deconvoluted into two components corresponding to C–Si–O and Si–O–Zr bonds, confirming the formation of a dual interfacial bonding network between KH-560, the polymer matrix, and LLZO particles (Figure 3E). After silane modification of LLZO, the Zr 3d binding energy exhibits a slight positive shift (Figure 3F), accompanied by the appearance of characteristic organosilicon signals in the Si 2p spectrum (Figure 3G). In the O 1s spectrum, the intensity of surface hydroxyl groups decreases while a new Si–O component emerges (Figure 3H), confirming that silanol groups generated from KH-560 hydrolysis undergo condensation reactions with surface hydroxyls of LLZO, forming stable Si–O–Zr linkages. Additionally, FTIR spectra (Figure S4) show characteristic absorption bands at 953 cm^{-1} and 1195 cm^{-1} for KH-560/LLZO, corresponding to Si–O–Zr and Si–O–C vibrations, respectively, further supporting the successful interfacial coupling.

DFT calculations further elucidate the interfacial strengthening mechanism from an energetic perspective (Figure S5). The binding energy between KH-560 and the LLZO surface is -102.4 $kJ{\cdot}mol^{-1}$, while that between KH-560 and the polyurethane segment is -81.07 $kJ{\cdot}mol^{-1}$, both significantly exceeding the typical range of physical adsorption, indicating the formation of stable chemical interactions within the system. The trend in binding energies suggests that the silane coupling agent preferentially anchors onto the LLZO surface and subsequently interacts with polymer segments, thereby constructing a continuous PU–Si–O–Zr–LLZO cross-phase network. Molecular electrostatic potential (ESP) analysis further reveals that silane bridging leads to a more homogeneous interfacial potential distribution across the composite system, effectively alleviating local charge accumulation and reducing interfacial energy.

Thermal Stability and Flame-Retardant Mechanism

First, thermogravimetric analysis (TGA) was conducted to investigate the thermal stability of PHB, PHBP and PHBP-LLZO. As shown in Figure 4A, all three membranes underwent rapid decomposition in the temperature range of 350-450 °C, with residual masses of 3.5%, 8.2% and 42.6% at 450 °C, respectively. The surfaces of the corresponding thermal decomposition residues were further examined by SEM-EDS (Figure S6). Numerous wrinkles were observed on the surface of the PHB residue (Figure S6A), whereas a porous phosphorus-containing carbonaceous residue layer was formed on the surface of PHBP (Figure S6B). In contrast, the PHBP-LLZO residue exhibited a relatively compact surface, with C, O, P, and Zr elements uniformly distributed throughout the residue (Figure S6C).

The glass-transition temperatures (Tg) of PHB, PHBP and PHBP-LLZO were −37.6, −48.8 and −49.3 °C, respectively (Figure 4B). The introduction of flexible disulfide bonds in BHDS, together with the disruption of hard-segment regularity by DOPO-HQ, contributed to the reduction in Tg of the membranes. Correspondingly, melting endothermic peaks were observed at approximately 30.1, 34.6 and 36.9 °C for the three samples, respectively. Thermomechanical analysis (TMA) in compression mode was further employed to evaluate the thermally induced dimensional changes of the membranes upon heating (Figure 4C). The PHB membrane began to soften at approximately 31 °C, followed by accelerated deformation above 114 °C. By comparison, PHBP showed observable deformation at 81 °C and exhibited rapid softening above 128 °C. For the PHBP-LLZO composite electrolyte, the thermally induced release of residual interfacial stress within the polymer-ceramic composite network resulted in its initial dimensional increase at relatively low temperatures. During membrane fabrication, the shrinkage of the polymer matrix was constrained by the rigid LLZO particles and their interfacial interactions, which induced residual stress accumulation at the polymer-ceramic interfaces. Upon heating, the enhanced chain mobility enabled the gradual relaxation of these interfacial stresses, giving rise to a transient dimensional recovery in the low-temperature region. With further heating, the polymer network gradually softened and eventually underwent thermal shrinkage. The softening temperature of PHBP-LLZO was approximately 124 °C, and its dimensional change reached -12 μm at 150 °C. These results indicate that the rigid LLZO phase and the strong interfacial interactions between LLZO and the polymer matrix effectively suppress large-scale ther-

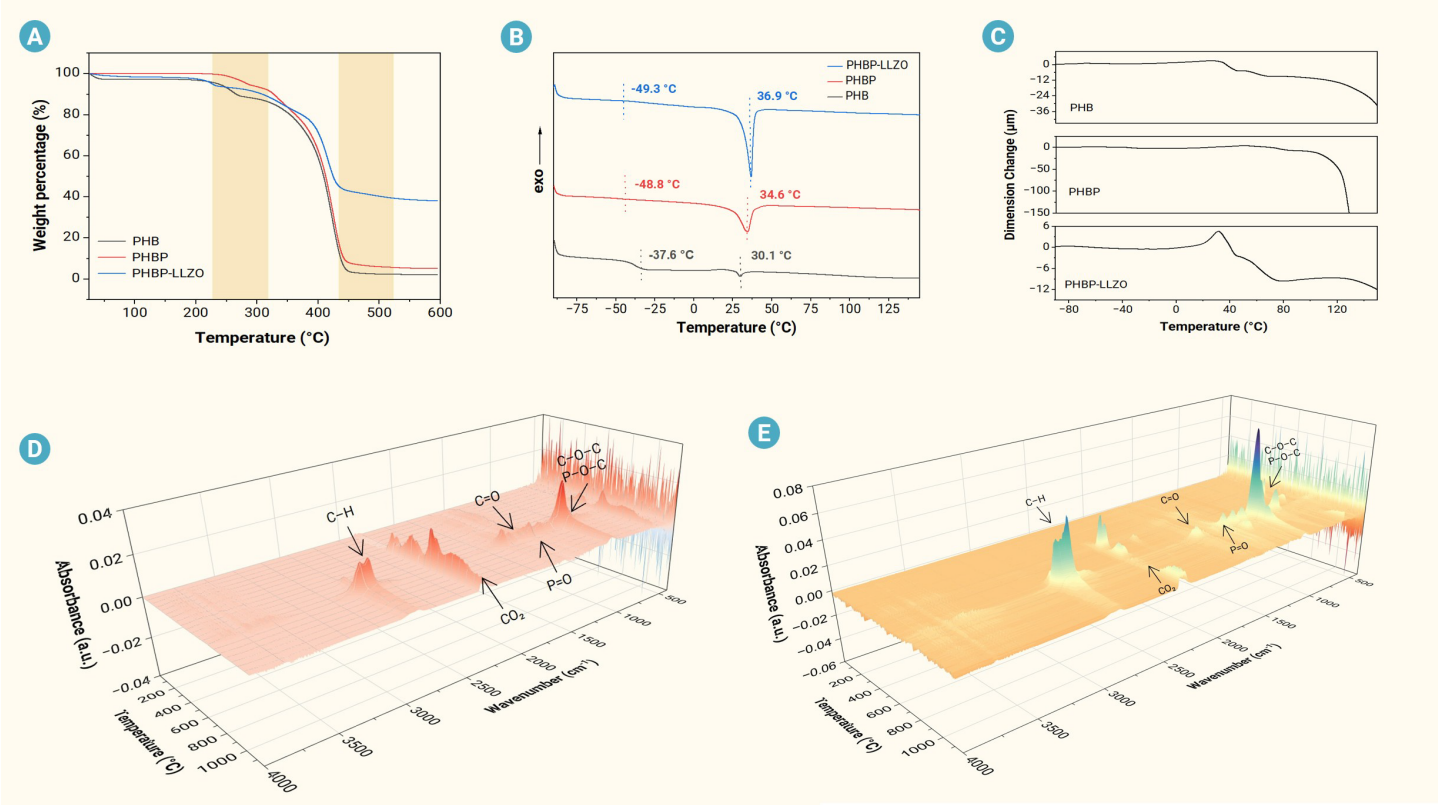


Figure 4. Thermal stability, thermomechanical behavior, and flame-retardant performance of PHB, PHBP and PHBP-LLZO (A) TGA curves; (B) DSC curves; (C) TMA curves; (D) 3D TG-IR spectrum of PHBP-LLZO; and (E) 3D TG-IR spectrum of PHBP.

mal deformation, thereby imparting excellent thermal dimensional stability to the composite electrolyte.

The flame-retardant behavior of the materials was further evaluated by direct combustion tests (Figure S7). Under flame exposure, PHB underwent sustained and vigorous combustion, whereas PHBP and PHBP-LLZO exhibited different degrees of combustion suppression. Notably, the PHBP-LLZO membrane largely retained its structural integrity after removal of the ignition source, indicating its superior flame-retardant performance. To elucidate the flame-retardant mechanisms of the different electrolyte membranes, thermogravimetric analysis coupled with Fourier transform infrared spectroscopy (TG-IR) was performed on all three membranes. During thermal decomposition, all three materials exhibited characteristic absorption bands at approximately 2930, 2350, and 1740 cm^{-1}, corresponding to aliphatic C-H stretching vibrations, CO_2, and carbonyl-containing volatile species, respectively. Compared with PHB (Figure S8), PHBP and PHBP-LLZO exhibited additional characteristic vibrational bands at approximately 1260 and 1100 cm^{-1}, which were assigned to P=O and P–O/P–O–C vibrations, respectively, indicating the participation of DOPO-HQ in the thermal decomposition process (Figure 4D & E).

Density functional theory (DFT) calculations were further conducted to elucidate the flame-retardant mechanism of DOPO-HQ (Figure S9). The homolytic bond dissociation enthalpy (BDE) of the P–C bond in DOPO-HQ was calculated to be 288 $kJ{\cdot}mol^{-1}$, which is significantly lower than that of the C–C (345 $kJ{\cdot}mol^{-1}$) and C–H (430 $kJ{\cdot}mol^{-1}$) bonds in the polymer backbone, indicating that the P–C bond is the preferential cleavage site under thermal stress. Geometry optimizations and electrostatic potential (ESP) analyses of DOPO-HQ and the corresponding radical species reveal pronounced redistribution of electron density after bond cleavage, generating highly reactive phosphorus-centered radicals. These species can migrate into the gas phase and effectively scavenge combustion radicals such as H• and OH•, thereby interrupting the chain reaction and suppressing flame propagation. As a result, the PHBP-LLZO composite membrane exhibits efficient gas-phase flame-retardant behavior.

Flexibility and Dynamic Healing Mechanism

Flexibility is a key advantage of composite solid electrolytes compared with inorganic counterparts. When subjected to external deformation or mechanical damage, electrolytes with shape recoverability and repairability are crucial for ensuring battery safety. The tensile strengths of PHB, PHBP, and PHBP-LLZO are 17.5, 13.9, and 19.8 MPa, respectively, while their elongation at break values are 1272%, 861%, and 988%, respectively (Figure 5A). Compared with pristine PHB, the PHBP membrane containing DOPO-HQ exhibits reduced tensile strength and ductility due to increased rigid segment content. In contrast, after incorporation of LLZO particles, the PHBP-LLZO membrane exhibits a significant enhancement in tensile strength, exceeding that of PHB, while maintaining a balanced elongation at break. This improvement is attributed to the formation of Si–O–Zr interfacial linkages, which reinforce interfacial load transfer and mechanical integrity within the composite.

The PHBP-LLZO membrane can be stretched from 3 cm to 16 cm without fracture (Figure 5B). Cyclic loading-unloading tests at 500% strain (Figure 5C) reveal pronounced hysteresis loops in each cycle, indicating significant energy dissipation during deformation. With increasing cycle number, the stress-strain curves gradually stabilize, suggesting good elastic recovery and structural robustness of the composite membrane. Notably, after being completely cut and thermally treated at 60 °C for 1 h, the PHBP-LLZO membrane exhibits effective self-healing behavior (Figure 5D). The healed membrane retains a tensile strength of 7.5 MPa and an elongation at break of 487% (Figure 5E). This self-healing capability originates from thermally activated reversible disulfide exchange reactions in the PHBP backbone, which facilitate chain diffusion and interfacial re-bonding across the damaged interface, enabling recovery of mechanical integrity.

During battery operation, the PHBP-LLZO membrane undergoes deformation in response to the strain imposed by electrode volume changes. The experimental results demonstrate that the material design adopted to prevent electrolyte membrane fracture effectively fulfills its intended role. The flexible PEG segments accommodate external strain through conformational changes. Meanwhile, the N–H groups of the urethane moieties in PHBP can form reversible N–H···O=C hydrogen bonds with carbonyl oxygen atoms on neighboring polymer chains. The chain segments containing P=O groups further enhance interchain interactions through N–H···O=P interactions, helping to maintain the integrity of the polymer network. In addition, the dynamic

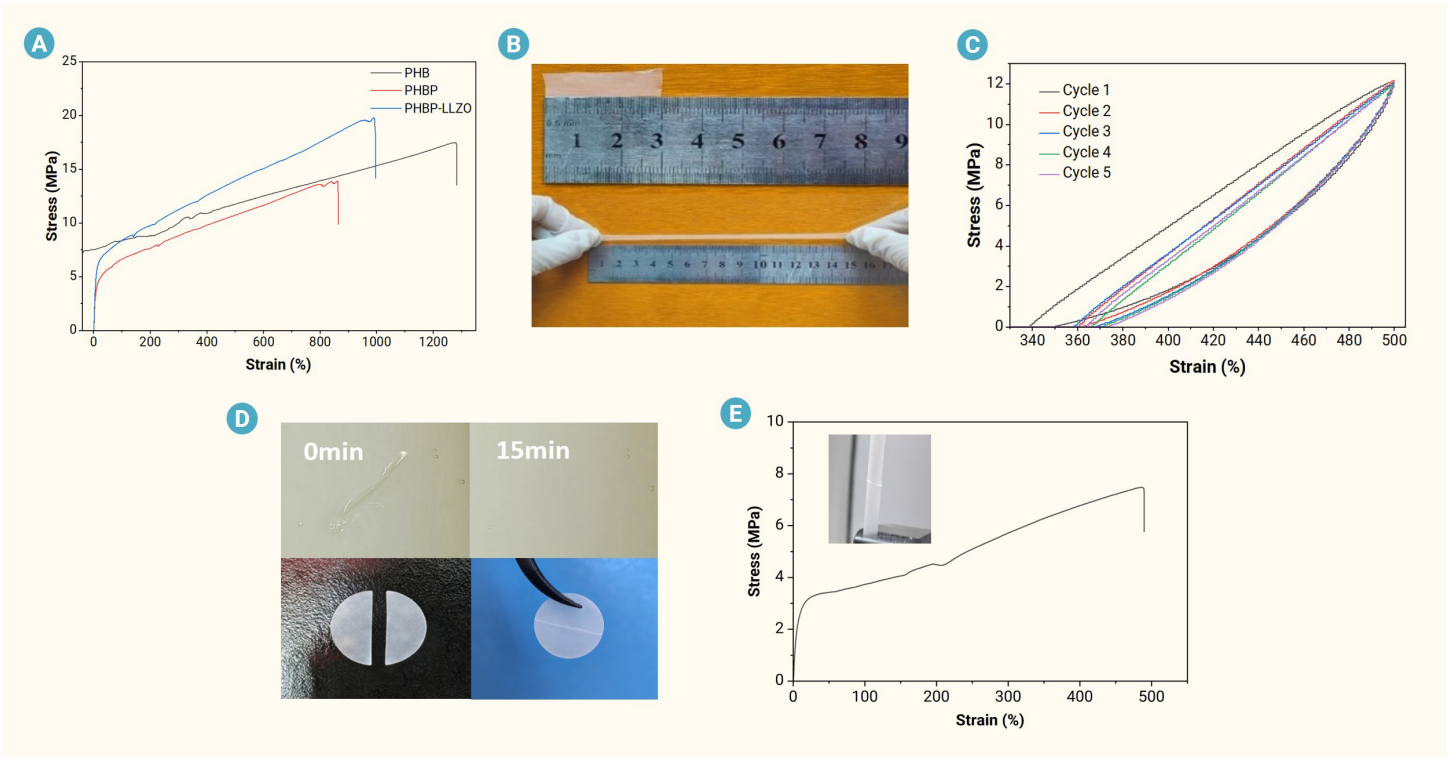


Figure 5. Mechanical and self-healing properties of the composite membranes (A) Stress-strain curves of PHB, PHBP, and PHBP-LLZO membranes; (B) macroscopic photograph of the PHBP-LLZO membrane under stretching, demonstrating its high flexibility; (C) cyclic loading-unloading curves of the PHBP-LLZO membrane at 500% strain; (D) optical images of the self-healing process, including surface scratch healing (top) and complete cut-and-healing behavior (bottom); (E) stress-strain curve of the healed composite membrane.

disulfide bonds can facilitate network reorganization through bond-exchange reactions under thermal activation. The (KH-560)-modified LLZO provides rigid reinforcement through Si–O–Zr interfacial linkages and organic-inorganic interactions, thereby suppressing excessive deformation of the polymer network.

Electrochemical Performance of the PHBP-LLZO Membrane

The optimal mass ratio of PHBP to LLZO in the PHBP-LLZO membrane was determined to be 6:4 based on the experiments shown in Figure S10 and Table S1. Symmetric cells were assembled using PHB, PHBP, and PHBP-LLZO electrolytes, and their ionic conductivities measured at 25 °C were 4.58 × 10^{-5}, 6.22 × 10^{-5} and 2.03 × 10^{-4} S·cm^{-1}, respectively (Figure 6A). Furthermore, the recovery of ionic conductivity after self-healing of the PHBP-LLZO membrane was evaluated. The ionic conductivity of the membrane after self-healing was 8.48 × 10^{-5} S·cm^{-1}, corresponding to a recovery ratio of 41.8% (Figure 6B).

The significantly enhanced conductivity of PHBP-LLZO highlights the synergistic contribution of the inorganic ion-conducting phase and the well-constructed organic-inorganic interface facilitated by KH-560. Temperature-dependent EIS measurements of the PHBP-LLZO membrane (Figure 6C) and the corresponding Arrhenius plot (Figure 6D) indicate that ion transport follows a typical thermally activated behavior. The PHBP-LLZO membrane exhibits a relatively low activation energy (E_a = 0.45 eV), suggesting that Li^+ migration is facilitated by the coupled effects of PEG segmental motion and interfacial conduction pathways provided by LLZO, thereby effectively reducing the migration energy barrier. Linear sweep voltammetry (LSV) results (Figure 6E) show that the PHB membrane exhibits an oxidation onset at 4.11 V, which shifts to 4.43 V for PHBP. This enhancement is attributed to the incorporation of rigid aromatic structures and P-O bonds from DOPO-HQ, which improve the oxidative stability of the polymer backbone. With further addition of LLZO, the electrochemical stability window is extended to 5.05 V, significantly outperforming both PHB and PHBP membranes. Meanwhile, the lithium-ion transference number of PHBP-LLZO reaches 0.58 (Figure 6F), markedly higher than that of PHB, which is 0.37 (Figure S11), indicating more efficient Li^+-dominated transport within the composite electrolyte.

To elucidate the ion transport mechanism, DFT calculations were performed to investigate the interactions between Li^+ and three functional units – PEG, DOPO-HQ, and BHDS (Figure S12). The calculated binding energies with Li^+ are -76.14, -186.41 and -89.27 kJ·mol^{-1}, respectively. PEG coordinates with Li^+ primarily through ether oxygen atoms in a single-site coordination mode, consistent with the typical transport mechanism of polyether-based electrolytes. In contrast, BHDS provides multi-site coordination through both hydroxyl groups and sulfur atoms, thereby enhancing its Li^+ affinity. DOPO-HQ exhibits the strongest interaction with Li^+, attributed to the high electron density of the P=O group together with auxiliary coordination from phenolic hydroxyl groups, forming a robust multi-site binding configuration. These results demonstrate that DOPO-HQ not only functions as a flame-retardant unit but also introduces additional strong coordination sites within the polymer matrix. Together with the auxiliary coordination contribution from BHDS, these functional units construct a multi-component Li^+ coordination network that operates synergistically with PEG-based transport pathways. This cooperative ion-coordination architecture provides a theoretical basis for the enhanced ionic conductivity observed in the PHBP-LLZO composite electrolyte.

Electrolyte Interfacial Stability and Quasi-Solid-State Battery Performance

LFP||Li coin cells were assembled with various electrolyte membranes to evaluate their rate and cycling performance (LFP cathode active-material loading: 2 mg·cm^{-2}). In the rate performance test (Figure 7A), the initial discharge specific capacities of the cells based on PHB, PHBP, and PHBP-LLZO electrolytes at 0.1 C were 142.4, 150.5, and 153.2 mAh·g^{-1}, respectively. As the rate increased from 0.1 C to 1 C, the capacities decreased to 73.3, 110.1, and 127.1 mAh·g^{-1}, respectively, while the PHBP-LLZO cell consistently delivered the highest capacity. When the rate was returned to 0.2 C and 0.1 C, the discharge capacity of the PHBP-LLZO cell recovered almost completely, indicating excellent rate reversibility and structural stability, and suggesting that LLZO inorganic pathways effectively supplement Li^+ transport at high rates, thereby alleviating concentration polarization. In the cycling test (Figure 7B), the PHB cell at 0.5 C exhibited rapid capacity fading within

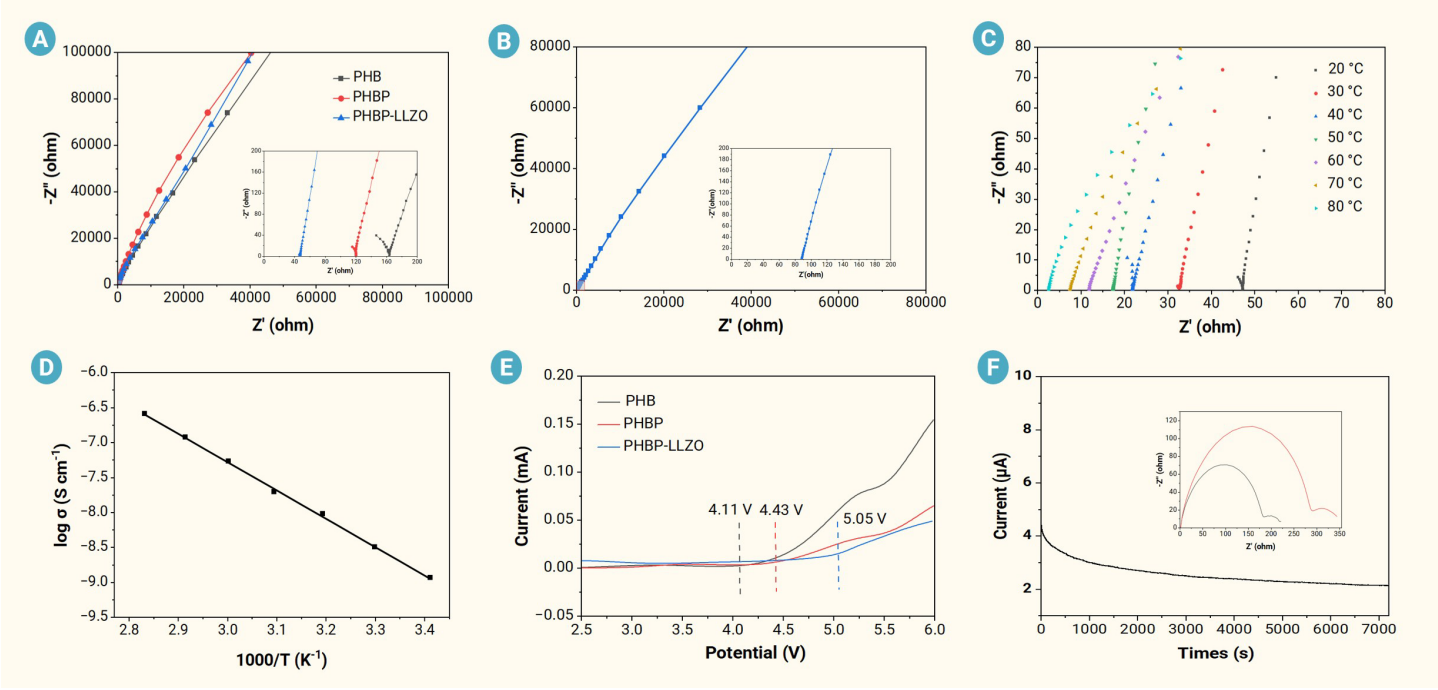


Figure 6. Ion transport properties and electrochemical stability of the PHBP-LLZO composite electrolyte (A) Nyquist plots of the different electrolyte membranes at 25 °C. (B) Nyquist plot of the PHBP-LLZO membrane after self-healing at 25 °C. (C) EIS spectra of the PHBP-LLZO composite membrane at various temperatures. (D) Arrhenius fitting curve of the ionic conductivity. (E) linear sweep voltammetry (LSV) curves. (F) chronoamperometry curve of the PHBP-LLZO membrane and the impedance spectra before and after polarization.

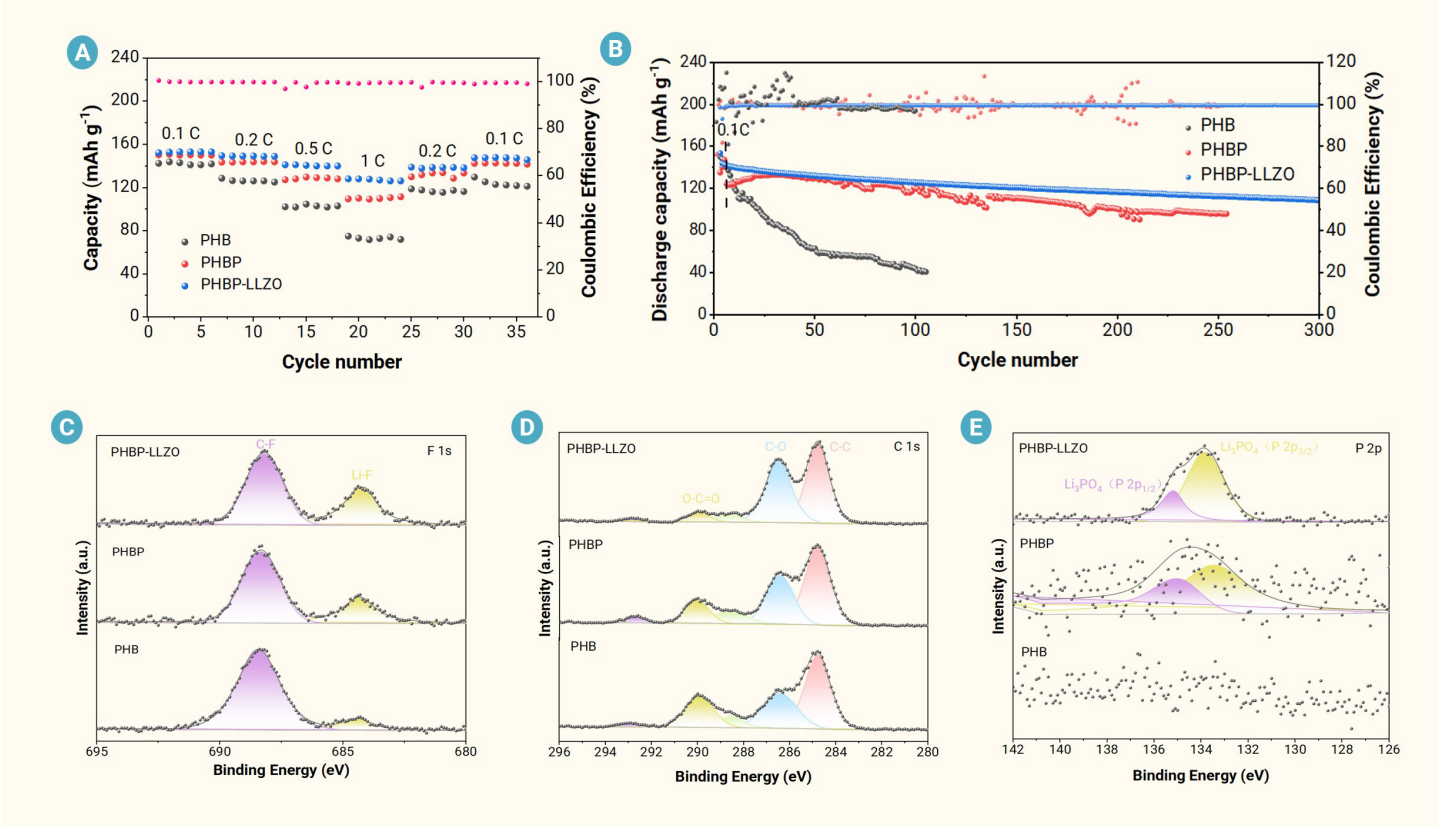


Figure 7. Performance of LFP||Li cells assembled with different electrolytes and interfacial composition of the Li anode after cycling (A) rate performance of the LFP||Li cells. (B) cycling performance at 0.5 C. XPS fine spectra of the Li anode surface after 100 cycles: (C) F 1s, (D) C 1s, (E) P 2p.

50 cycles, retaining only 30.5% (42.8 mAh·g^{-1}) after 100 cycles. The PHBP cell showed improved stability, retaining 65.2% (96.3 mAh·g^{-1}) after 250 cycles. Notably, the PHBP-LLZO cell delivered an initial capacity of 156.6 mAh·g^{-1}, exhibited stable capacity retention, and maintained 70.3% (110.2 mAh·g^{-1}) capacity retention after 300 cycles with nearly 100% Coulombic efficiency. When the cathode active-material loading was increased to 4 mg·cm^{-2}, the three cells exhibited decreased initial specific capacities, while their other electrochemical performance characteristics remained comparable to those observed at a cathode loading of 2 mg·cm^{-2} (Figure S13).

Subsequently, constant-current cycling of Li||Li symmetric cells at 0.1

mA·cm^{-2} was conducted to evaluate interfacial stability (Figure S14). The PHB cell exhibited a relatively high initial polarization, which continuously increased during cycling, indicating interfacial instability and non-uniform Li deposition. In contrast, the PHBP cell containing DOPO-HQ showed a significantly reduced and stable polarization voltage. Notably, the PHBP-LLZO cell maintained an ultralow polarization voltage of ~0.01 V over 1200 h, confirming the stable PHBP-LLZO/Li interface.

A cell using the self-healed PHBP-LLZO membrane was reassembled, and EIS measurements revealed an interfacial resistance of 18.14 Ω, which was 6.40 Ω higher than that measured the cell before self-healing, indicating that the interfacial ion-transport performance between the electrolyte and electrode was moderately affected by the self-healing process (Figure S15). Galvanostatic cycling results (Figure S16) showed that no continuous increase in polarization or short circuit occurred over 560 h at a current density of 0.1 mA·cm^{-2}, demonstrating good interfacial stability. Furthermore, the LFP||Li half-cell employing the self-healed PHBP-LLZO membrane with a cathode active-material loading of 2 mg·cm^{-2} delivered a discharge capacity of 109.7 mAh·g^{-1} after 60 cycles at 60 °C, corresponding to a capacity retention of 73.2% (Figure S17).

To further analyze the interfacial chemistry after cycling, XPS measurements were performed on Li anodes after 100 cycles. In the F 1s spectra (Figure 7C), peaks at 684.2 eV (LiF) and 688.2 eV (fluorinated species from $TFSI^-$ decomposition) are observed. Compared with PHB and PHBP, the PHBP-LLZO anode exhibits a stronger LiF signal, suggesting the formation of a more LiF-rich SEI layer, which enhances interfacial stability. In the C 1s spectra (Figure 7D), the intensity of O–C=O (289.9 eV) species is reduced in PHBP/LLZO, indicating suppressed decomposition of organic components due to the protective effect of the ceramic interface. In the P 2p spectra (Figure 7E), a peak at 133.4 eV corresponding to phosphate species (Li_3PO_4/Li_xPO_y) is observed, suggesting participation of DOPO-HQ in SEI formation. In addition, S 2p and N 1s spectra (Figure S18) indicate that LiTFSI-derived species contribute to SEI construction and that the interfacial chemical environment is more uniform in the PHBP-LLZO system after cycling.

SEM images further reveal the morphological evolution of Li anodes after cycling (Figure S19). The PHB-based Li anode exhibits a porous and irregular surface, indicating severe side reactions and non-uniform Li deposition. The PHBP-based Li anode becomes relatively denser but still shows localized cracks. In contrast, the (PHBP-LLZO)-based Li anode is smooth and homogeneous without obvious dendritic structures, demonstrating effective suppression of Li dendrite growth and uniform Li deposition. The cross-section images of the LFP cathode/electrolyte revealed that the electrolyte layer in the PHB-based cell was relatively nonuniform, accompanied by an irregular structure in cathode side. In the PHBP-based cell, obvious cracks were observed in both the electrolyte and cathode layer. In contrast, the electrolyte and cathode layer remained relatively intact and well-structured in the (PHBP-LLZO)-based cell, indicating that the composite electrolyte was capable of maintaining more stable electrode/electrolyte contact during cycling (Figure S20).

CONCLUSION

The functionalized polyurethane matrix PHBP, constructed from PEG2000, HDI, BHDS, and DOPO-HQ, exhibits a favorable combination of flexibility, self-healing capability, and flame retardancy. After KH-560 modification, PHBP was composited with LLZO at a weight ratio of 6:4. KH-560 forms Si–O–Zr covalent linkages with LLZO while also interacting with the polymer matrix (PHBP) through non-covalent interactions, primarily hydrogen bonding, thereby acting as a molecular bridge that enhances organic-inorganic interfacial compatibility. The resulting PHBP-LLZO composite electrolyte delivers a room-temperature ionic conductivity of 2.03 × 10^{-4} S·cm^{-1}, a lithium-ion transference number of 0.58, and an expanded electrochemical stability window of 5.05 V. In addition, it exhibits excellent flame retardancy and enables rapid self-healing at 60 °C. The LFP||Li cell assembled with this electrolyte retains 70.3% capacity after 300 cycles at 0.5 C, while the Li||Li symmetric cell maintains stable cycling for over 1200 h. These results demonstrate that the composite electrolyte effectively suppresses lithium dendrite growth and significantly enhances electrode/electrolyte interfacial stability, providing valuable insights into the design of high-safety and long-life solid-state lithium metal batteries.

REFERENCES

1. Huo S., Sheng L., Xue W., et al. (2023). Challenges of polymer electrolyte with wide electrochemical window for high energy solid-state lithium batteries. *InfoMat.* **5**:e12394. DOI:10.1002/inf2.12394
2. Ke X. Y., Wang Y., Ren G. F., et al. (2020). Towards rational mechanical design of inorganic solid electrolytes for all-solid-state lithium ion batteries. *Energy Storage Mater.* **26**:313–324. DOI:10.1016/j.ensm.2019.08.029
3. Zhao W. J., Yi J., He P., et al. (2019). Solid-State Electrolytes for Lithium-Ion Batteries: Fundamentals, Challenges and Perspectives. *Electrochem. Energy Rev.* **2**:574–605. DOI:10.1007/s41918-019-00048-0
4. Li Q., Yu X., Li H., et al., (2024). The road towards high-energy-density batteries. *Innov. Energy* **1**: 100005. DOI:10.59717/j.xinn-energy.2024.100005.
5. Sarfraz N., Kanwal N., Ali M., et al. (2024). Materials advancements in solid-state inorganic electrolytes for highly anticipated all solid Li-ion batteries. *Energy Storage Mater.* **71**:103619. DOI:10.1016/j.ensm.2024.103619
6. Yu T., Liu Y. K., Li H. Y., et al. (2025). Ductile Inorganic Solid Electrolytes for All-Solid-State Lithium Batteries. *Chem. Rev.* **125**:3595–3662. DOI:10.1021/acs.chemrev.4c00894
7. Han X., Xu Y., Li H. M., et al. (2025). Mechanically robust halide electrolytes for high-performance all-solid-state batteries. *Nat. Commun.* **16**:9770. DOI:10.1038/s41467-025-64726-y
8. Shen X. H., Zhang L. Q., Zhu J., et al. (2025). Super electrolyte-philic all-inorganic ceramic separators for highly robust lithium batteries. *Energy Storage Mater.* **80**:104389. DOI:10.1016/j.ensm.2025.104389
9. Lu X., Wang Y. M., Xu X. Y., et al. (2023). Polymer-Based Solid-State Electrolytes for High-Energy-Density Lithium-Ion Batteries-Review. *Adv. Energy Mater.* **13**:2301746. DOI:10.1002/aenm.202301746
10. Song Z. Y., Chen F. F., Martinez-Ibañez M., et al. (2023). A reflection on polymer electrolytes for solid-state lithium metal batteries. *Nat. Commun.* **14**:4884. DOI:10.1038/s41467-023-40609-y
11. Yi X. P., Yang Y., Xiao K. S., et al. (2025). Achieving Balanced Performance and Safety for Manufacturing All-Solid-State Lithium Metal Batteries by Polymer Base Adjustment. *Adv. Energy Mater.* **15**:2404973. DOI:10.1002/aenm.202404973
12. Cheng Z. W., Liu T., Zhao B., et al. (2021). Recent advances in organic-inorganic composite solid electrolytes for all-solid-state lithium batteries. *Energy Storage Mater.* **34**:388–416. DOI:10.1016/j.ensm.2020.09.016
13. Maurya D. K., Bazri B., Srivastava P., et al. (2024). Ceramic Rich Composite Electrolytes: An Overview of Paradigm Shift toward Solid Electrolytes for High-Performance Lithium-Metal Batteries. *Adv. Energy Mater.* **14**:2402402. DOI:10.1002/aenm.202402402
14. Daems K., Yadav P., Dermenci K. B., et al. (2024). Advances in inorganic, polymer and composite electrolytes: Mechanisms of Lithium-ion transport and pathways to enhanced performance. *Renew Sustain Energy Rev.* **191**:114136. DOI:10.1016/j.rser.2023.114136
15. Dirican M., Yan C. Y., Zhu P., et al. (2019). Composite solid electrolytes for all-solid-state lithium batteries. *Mater. Sci. Eng. R Rep.* **136**:27–46. DOI:10.1016/j.mser.2018.10.004
16. Wang S. H., La Monaca A. and Demopoulos G. P. (2025). Composite solid-state electrolytes for all solid-state lithium batteries: progress, challenges and outlook. *Energy Adv.* **4**:11–36. DOI:10.1039/d4ya00542b
17. Zhang X. R., Liu S. Y., Sun Y. X., et al. (2024). Surface Coordination of Garnet Fillers Improves the Organic-Inorganic Interfacial Compatibility of Composite Solid Electrolyte. *Small* **20**:2405909. DOI:10.1002/smll.202405909
18. Fu J., Li Z., Zhou X., et al. (2022). Ion transport in composite polymer electrolytes. *Mater. Adv.* **3**:3809–3819. DOI:10.1039/d2ma00215a
19. Song Y. X., Su M., Xiang H. Y., et al. (2025). PEO-Based Solid-State Polymer Electrolytes for Wide-Temperature Solid-State Lithium Metal Batteries. *Small* **21**:2408045. DOI:10.1002/smll.202408045
20. Zhang X. Y., Fu C. K., Cheng S. C., et al. (2023). Novel PEO-based composite electrolyte for low-temperature all-solid-state lithium metal batteries enabled by interfacial cation-assistance. *Energy Storage Mater.* **56**:121–131. DOI:10.1016/j.ensm.2022.12.048
21. He C. W., Ying H. J., Cai L. C., et al. (2024). Tailoring Stable PEO-Based Electrolyte/Electrodes Interfaces via Molecular Coordination Regulating Enables 4.5 V Solid-State Lithium Metal Batteries. *Adv. Funct. Mater.* **34**:2410350. DOI:10.1002/adfm.202410350.
22. Zhang C. H., Zhao L. W., Li F. K., et al. (2025). Optimizing the Electron Density of PVDF-HFP-Based Solid Polymer Electrolyte by Donor-Acceptor COF Toward High-Performance Solid-State Lithium Metal Batteries. *Adv. Mater.* **37**:e13427. DOI:10.1002/adma.202513427
23. Lu J. J., Sheng B. F., Chen M. F., et al. (2024). Localized high concentration polymer electrolyte enabling room temperature solid-state lithium metal batteries with stable LiF-rich interphases. *Energy Storage Mater.* **71**:103570. DOI:10.1016/j.ensm.2024.103570
24. Yang W. J., Liu Y. W., Sun X. Y., et al. (2024). Solvation-Tailored PVDF-Based Solid-

State Electrolyte for High-Voltage Lithium Metal Batteries. *Angew. Chem. Int. Ed.* **63**:e202401428. DOI:10.1002/anie.202401428
25. Liu Y., Zhang S. Y., Zhang N., et al. (2026). Dipole competition-driven reconstructing helical conformations of PAN polymer electrolytes for enhanced ionic transport capability. *Energy Storage Mater.* **84**:104809. DOI:10.1016/j.ensm.2025.104809
26. Yan R., Zhang K. Y., Li B. B., et al. (2025). Nitrile-based solid polymer electrolytes for novel energy storage systems: A perspective from ion transport mechanism to applications in solid-state batteries. *Energy Storage Mater.* **79**:104317. DOI:10.1016/j.ensm.2025.104317
27. Yang J. Y., Cao Z., Chen Y. W., et al. (2023). Dry-Processable Polymer Electrolytes for Solid Manufactured Batteries. *ACS Nano.* **17**:19903–19913. DOI:10.1021/acsnano.3c04610
28. Man B., Zhao Y., Fu B., et al. (2026). Multifunctional Design of Solid Polymer Electrolytes: Paving the Way for High-Performance All-Solid-State Batteries. *Carbon Energy.* **0**:1–98. DOI:10.1002/cey2.70188
29. Chattopadhyay J., Pathak T. S. and Santos D. M. F. (2023). Applications of Polymer Electrolytes in Lithium-Ion Batteries: A Review. *Polymers* **15**:3907. DOI:10.3390/polym15193907
30. Tong R. A., Huang Y. L., Feng C., et al. (2024). In-Situ Polymerization Confined PEGDME-Based Composite Quasi-Solid-State Electrolytes for Lithium Metal Batteries. *Adv. Funct. Mater.* **34**:2315777. DOI:10.1002/adfm.202315777
31. Wang C., Hu Z. Y., Zhu C. X., et al. (2025). Tailoring lithium-ion transport for dendrite-free PEO-based composite electrolyte. *Chem. Eng. J.* **520**:166014. DOI:10.1016/j.cej.2025.166014
32. Feng J., Wang L., Chen Y., et al. (2021). PEO based polymer-ceramic hybrid solid electrolytes: a review. *Nano Converg.* **8**:2. DOI:10.1186/s40580-020-00252-5
33. Lv Z. L., Tang Y., Dong S. M., et al. (2022). Polyurethane-based polymer electrolytes for lithium Batteries: Advances and perspectives. *Chem. Eng. J.* **430**:132659. DOI:10.1016/j.cej.2021.132659
34. Dai D. M., Yan P. Y., Liu D. H., et al. (2025). Hydrogen Bonds Boost Lithium Salt Dissociation in Composite Solid-State Electrolyte: Enhanced Cycling Life of Lithium Metal Batteries. *Adv. Funct. Mater.* **35**:2503696. DOI:10.1002/adfm.202503696
35. Zhang Q., Wen Y. H., Liu K., et al. (2021). Study of solid polyurethane electrolytes synthesized from HDI and PEO of different molecular weight. *J. Electroanal. Chem.* **893**:115305. DOI:10.1016/j.jelechem.2021.115305
36. Cui P., Li Y. F., Liu Y. X., et al. (2024). Polyether-based polyurethane electrolyte for lithium metal battery: a perspective. *RSC Adv.* **14**:36152–36160. DOI:10.1039/d4ra06863g
37. Wu L., Pei F., Cheng D. M., et al. (2024). Flame-Retardant Polyurethane-Based Solid-State Polymer Electrolytes Enabled by Covalent Bonding for Lithium Metal Batteries. *Adv. Funct. Mater.* **34**:2310084. DOI:10.1002/adfm.202310084
38. Wang H. H., Li X. N., Zeng Q. H., et al. (2024). A novel hyperbranched polyurethane solid electrolyte for room temperature ultra-long cycling lithium-ion batteries. *Energy Storage Mater.* **66**:103188. DOI:10.1016/j.ensm.2024.103188
39. Gao Y. Q., Wang C. L., Wang H. R., et al. (2023). Polyurethane/LLZTO solid electrolyte with excellent mechanical strength and electrochemical property for advanced lithium metal battery. *Chem. Eng. J.* **474**:145446. DOI:10.1016/j.cej.2023.145446
40. Huang D. R., Wu L., Kang Q., et al. (2024). Amino-modified UiO-66-NH_2 reinforced polyurethane based polymer electrolytes for high-voltage solid-state lithium metal batteries. *Nano Res.* **17**:9662–9670. DOI:10.1007/s12274-024-6886-9
41. Elizalde F., Amici J., Trano S., et al. (2022). Self-healable dynamic poly(urea-urethane) gel electrolyte for lithium batteries. *J. Mater. Chem. A* **10**:12588–12596. DOI:10.1039/d2ta02239g
42. Li Y. X., Wu Y. J., Wang Z. X., et al. (2022). Progress in solvent-free dry-film technology for batteries and supercapacitors. *Mater. Today* **55**:92–109. DOI:10.1016/j.mattod.2022.04.008
43. Ludwig B., Pan H., Liu J., et al. (2017). Powder-based Additive Manufacturing of Li-ion Batteries and Micropowder Mixing Characteristics. *In: Proceedings of the 12th ASME International Manufacturing Science and Engineering Conference*, Los Angeles, CA, USA. https://doi.org/10.1115/MSEC2017-2900.
44. Zhang Z. Y., Zhang S., Geng S. X., et al. (2022). Agglomeration-free composite solid electrolyte and enhanced cathode-electrolyte interphase kinetics for all-solid-state lithium metal batteries. *Energy Storage Mater.* **51**:19–28. DOI:10.1016/j.ensm.2022.06.025
45. Zhang C., Wang Y. and Sun H. (2025). Dry-coating electrode fabrication for sustainable, high-performance batteries. *Sci. China Chem.* **68**:6391–6402. DOI:10.1007/s11426-025-3119-x
46. Liu J. N., Cao J. H., Wu Y. Y., et al. (2025). Micro porous forming of polyimide composite membrane with temperature and humidity control and its application Evaluation in lithium-ion batteries. *J. Power Sources* **644**:237082. DOI:10.1016/j.jpowsour.2025.237082
47. Liu J. N., Cao J. H., Liang W. H., et al. (2022). PI-LAGP Separator-Construction, Battery Application Performance, and Chemical Valence Changes of Germanium. *ACS Appl. Polym. Mater.* **4**:4003–4012. DOI:10.1021/acsapm.2c00467
48. Lu T. and Chen F. W. (2012). Multiwfn: A multifunctional wavefunction analyzer. *J. Comput. Chem.* **33**:580–592. DOI:10.1002/jcc.22885
49. Humphrey W., Dalke A. and Schulten K. (1996). VMD: Visual molecular dynamics. *J. Mol. Graph.* **14**:33–38. DOI:10.1016/0263-7855(96)00018-5
50. Zhang L.-P., Zhao Z.-G., Huang Y.-Y., et al. (2024). Synergetic improvement of flame retardancy and heat resistance of cationic waterborne polyurethanes by introducing a DOPO-containing flame retardant. *Prog. Org. Coat.* **194**:108613. DOI:10.1016/j.porgcoat.2024.108613

FUNDING AND ACKNOWLEDGMENTS

This work was financially supported by the National Key R&D Pilot Project "Research and development of high temperature resistant, long life and high safety lithium batteries" (2022YFE0207300).

AUTHOR CONTRIBUTIONS

Ke-Xin Huang: Methodology, Investigation, Formal analysis, Validation, Visualization, Writing – original draft. Da-Yong Wu: Conceptualization, Writing – review & editing, Supervision, Resources, Funding acquisition, Project administration. Jian-Hua Cao: Writing – review & editing, Supervision, Project administration. Yue Li: Writing – review & editing, Supervision. Jun Shen: Funding acquisition, Resources.

DECLARATION OF INTERESTS

Jun Shen is an Editorial Board member of The Innovation Energy and was blinded from reviewing or making final decisions on the manuscript. Peer review was handled independently of this member and their research group. The other authors declare no conflicts of interest.

DATA AND CODE AVAILABILITY

Data are available from the corresponding author upon reasonable request.

SUPPLEMENTAL INFORMATION

It can be found online at https://doi.org/10.59717/j.xinn-energy.2026.100193